Biomedical Optics EXPRESS

# Optical imaging of resting-state functional connectivity in a novel arterial stiffness model

**Edgar Guevara,[1,2] Nataliya Sadekova,[3] Hélène Girouard,[3] and Frédéric Lesage[1,2,*]**

[1]*Department of Electrical Engineering, École Polytechnique de Montréal, 2500 Chemin de Polytechnique, Montréal, Qc, H3C 3A7 Canada*

[2]*Research Center, Montreal Heart Institute, 5000 Bélanger Est, Montréal, Qc, H3T 1J4, Canada*

[3]*Department of Pharmacology, Faculty of Medicine, Université de Montréal, 2900 Édouard-Montpetit Montréal, Qc, H3T 1J4 Canada*

[*]*frederic.lesage@polymtl.ca*

**Abstract:** This study aims to assess the impact of unilateral increases in carotid stiffness on cortical functional connectivity measures in the resting state. Using a novel animal model of induced arterial stiffness combined with optical intrinsic signals and laser speckle imaging, resting state functional networks derived from hemodynamic signals are investigated for their modulation by isolated changes in stiffness of the right common carotid artery. By means of seed-based analysis, results showed a decreasing trend of homologous correlation in the motor and cingulate cortices. Furthermore, a graph analysis indicated a randomization of the cortex functional networks, suggesting a loss of connectivity, more specifically in the motor cortex lateral to the treated carotid, which however did not translate in differentiated metabolic activity.



**OCIS codes:** (110.4234) Multispectral and hyperspectral imaging; (110.6150) Speckle imaging.

## References and links

1. World Health Organization, *World Health Statistics 2012* (WHO Press, 2012).
2. R. O. Roberts, D. S. Knopman, Y. E. Geda, R. H. Cha, V. L. Roger, and R. C. Petersen, "Coronary heart disease is associated with non-amnestic mild cognitive impairment," Neurobiol. Aging **31**(11), 1894–1902 (2010).
3. M. K. Aronson, W. L. Ooi, H. Morgenstern, A. Hafner, D. Masur, H. Crystal, W. H. Frishman, D. Fisher, and R. Katzman, "Women, myocardial infarction, and dementia in the very old," Neurology **40**(7), 1102–1106 (1990).
4. M. M. Breteler, J. J. Claus, D. E. Grobbee, and A. Hofman, "Cardiovascular disease and distribution of cognitive function in elderly people: the Rotterdam Study," BMJ **308**(6944), 1604–1608 (1994).
5. A. Singh-Manoux, A. R. Britton, and M. Marmot, "Vascular disease and cognitive function: evidence from the Whitehall II Study," J. Am. Geriatr. Soc. **51**(10), 1445–1450 (2003).
6. M. P. Pase, A. Herbert, N. A. Grima, A. Pipingas, and M. F. O'Rourke, "Arterial stiffness as a cause of cognitive decline and dementia: a systematic review and meta-analysis," Intern. Med. J. **42**(7), 808–815 (2012).
7. E. L. Glisky, "Changes in Cognitive Function in Human Aging," in *Brain Aging: Models, Methods, and Mechanisms.*, D. Riddle, ed. (CRC Press, 2007).
8. J. Sun, S. Tong, and G.-Y. Yang, "Reorganization of Brain Networks in Aging and Age-related Diseases," Aging Dis. **3**, 181–193 (2011).
9. C. Iadecola, "The overlap between neurodegenerative and vascular factors in the pathogenesis of dementia," Acta Neuropathol. **120**(3), 287–296 (2010).
10. B. H. Anderton, "Ageing of the brain," Mech. Ageing Dev. **123**(7), 811–817 (2002).
11. R. S. Marshall and R. M. Lazar, "Pumps, aqueducts, and drought management: vascular physiology in vascular cognitive impairment," Stroke **42**(1), 221–226 (2011).
12. R. S. Marshall, R. M. Lazar, J. Pile-Spellman, W. L. Young, D. H. Duong, S. Joshi, and N. Ostapkovich, "Recovery of brain function during induced cerebral hypoperfusion," Brain **124**(6), 1208–1217 (2001).
13. F. M. Faraci, "Protecting against vascular disease in brain," Am. J. Physiol. Heart Circ. Physiol. **300**(5), H1566–H1582 (2011).
14. V. Bolduc, E. Baraghis, N. Duquette, N. Thorin-Trescases, J. Lambert, F. Lesage, and E. Thorin, "Catechin prevents severe dyslipidemia-associated changes in wall biomechanics of cerebral arteries in LDLr–/–:hApoB+/+ mice and improves cerebral blood flow," Am. J. Physiol. Heart Circ. Physiol. **302**(6), H1330–H1339 (2012).

#191636 - $15.00 USD Received 3 Jun 2013; revised 4 Sep 2013; accepted 5 Sep 2013; published 4 Oct 2013

15. D. A. Gusnard and M. E. Raichle, "Searching for a baseline: functional imaging and the resting human brain," Nat. Rev. Neurosci. **2**(10), 685–694 (2001).
16. M. D. Greicius, B. Krasnow, A. L. Reiss, and V. Menon, "Functional connectivity in the resting brain: a network analysis of the default mode hypothesis," Proc. Natl. Acad. Sci. U.S.A. **100**(1), 253–258 (2003).
17. M. D. Fox and M. E. Raichle, "Spontaneous fluctuations in brain activity observed with functional magnetic resonance imaging," Nat. Rev. Neurosci. **8**(9), 700–711 (2007).
18. M. P. van den Heuvel and H. E. Hulshoff Pol, "Exploring the brain network: A review on resting-state fMRI functional connectivity," Eur. Neuropsychopharmacol. **20**(8), 519–534 (2010).
19. D. M. Cole, S. M. Smith, and C. F. Beckmann, "Advances and pitfalls in the analysis and interpretation of resting-state FMRI data," Front Syst Neurosci **4**, 8 (2010).
20. R. L. Buckner, J. R. Andrews-Hanna, and D. L. Schacter, "The brain's default network: anatomy, function, and relevance to disease," Ann. N. Y. Acad. Sci. **1124**(1), 1–38 (2008).
21. T. Gili, M. Cercignani, L. Serra, R. Perri, F. Giove, B. Maraviglia, C. Caltagirone, and M. Bozzali, "Regional brain atrophy and functional disconnection across Alzheimer's disease evolution," J. Neurol. Neurosurg. Psychiatry **82**(1), 58–66 (2011).
22. M. D. Greicius, G. Srivastava, A. L. Reiss, and V. Menon, "Default-mode network activity distinguishes Alzheimer's disease from healthy aging: evidence from functional MRI," Proc. Natl. Acad. Sci. U.S.A. **101**(13), 4637–4642 (2004).
23. Y. He, Z. Chen, G. Gong, and A. Evans, "Neuronal networks in Alzheimer's disease," Neuroscientist **15**(4), 333–350 (2009).
24. Y. Sun, L. Qin, Y. Zhou, Q. Xu, L. Qian, J. Tao, and J. Xu, "Abnormal functional connectivity in patients with vascular cognitive impairment, no dementia: a resting-state functional magnetic resonance imaging study," Behav. Brain Res. **223**(2), 388–394 (2011).
25. A. G. van Norden, K. F. de Laat, R. A. Gons, I. W. van Uden, E. J. van Dijk, L. J. van Oudheusden, R. A. Esselink, B. R. Bloem, B. G. van Engelen, M. J. Zwarts, I. Tendolkar, M. G. Olde-Rikkert, M. J. van der Vlugt, M. P. Zwiers, D. G. Norris, and F.-E. de Leeuw, "Causes and consequences of cerebral small vessel disease. The RUN DMC study: a prospective cohort study. Study rationale and protocol," BMC Neurol. **11**(1), 29 (2011).
26. H.-L. Cheng, C.-J. Lin, B.-W. Soong, P.-N. Wang, F.-C. Chang, Y.-T. Wu, K.-H. Chou, C.-P. Lin, P.-C. Tu, and I.-H. Lee, "Impairments in cognitive function and brain connectivity in severe asymptomatic carotid stenosis," Stroke **43**(10), 2567–2573 (2012).
27. N. Sadekova, D. Vallerand, E. Guevara, F. Lesage, and H. Girouard, "Carotid calcification in mice: a new model to study the effects of arterial stiffness on the brain," J Am Heart Assoc. Manuscript ID JAHA/2013/000224–T2 (posted May 17 2013, in press).
28. O. Moldestad, P. Karlsen, S. Molden, and J. F. Storm, "Tracheotomy improves experiment success rate in mice during urethane anesthesia and stereotaxic surgery," J. Neurosci. Methods **176**(2), 57–62 (2009).
29. A. K. Dunn, A. Devor, H. Bolay, M. L. Andermann, M. A. Moskowitz, A. M. Dale, and D. A. Boas, "Simultaneous imaging of total cerebral hemoglobin concentration, oxygenation, and blood flow during functional activation," Opt. Lett. **28**(1), 28–30 (2003).
30. S. Dubeau, G. Ferland, P. Gaudreau, E. Beaumont, and F. Lesage, "Cerebrovascular hemodynamic correlates of aging in the Lou/c rat: A model of healthy aging," Neuroimage **56**(4), 1892–1901 (2011).
31. D. T. Delpy, M. Cope, P. van der Zee, S. Arridge, S. Wray, and J. Wyatt, "Estimation of optical pathlength through tissue from direct time of flight measurement," Phys. Med. Biol. **33**(12), 1433–1442 (1988).
32. A. K. Dunn, A. Devor, A. M. Dale, and D. A. Boas, "Spatial extent of oxygen metabolism and hemodynamic changes during functional activation of the rat somatosensory cortex," Neuroimage **27**(2), 279–290 (2005).
33. M. Kohl, U. Lindauer, G. Royl, M. Kuhl, L. Gold, A. Villringer, and U. Dirnagl, "Physical model for the spectroscopic analysis of cortical intrinsic optical signals," Phys. Med. Biol. **45**(12), 3749–3764 (2000).
34. S. Prahl, "Optical Absorption of Hemoglobin," *http://omlc.ogi.edu/spectra/hemoglobin/*.
35. N. Brieu, E. Beaumont, S. Dubeau, J. Cohen-Adad, and F. Lesage, "Characterization of the hemodynamic response in the rat lumbar spinal cord using intrinsic optical imaging and laser speckle," J. Neurosci. Methods **191**(2), 151–157 (2010).
36. A. K. Dunn, H. Bolay, M. A. Moskowitz, and D. A. Boas, "Dynamic Imaging of Cerebral Blood Flow Using Laser Speckle," J. Cereb. Blood Flow Metab. **21**, 195–201 (2001).
37. D. A. Boas and A. K. Dunn, "Laser speckle contrast imaging in biomedical optics," J. Biomed. Opt. **15**(1), 011109 (2010).
38. J. D. Briers, "Laser Doppler, speckle and related techniques for blood perfusion mapping and imaging," Physiol. Meas. **22**(4), R35–R66 (2001).
39. J. Luckl, W. Baker, Z.-H. Sun, T. Durduran, A. G. Yodh, and J. H. Greenberg, "The biological effect of contralateral forepaw stimulation in rat focal cerebral ischemia: a multispectral optical imaging study," Front Neuroenergetics **2**, pii: 19 (2010).
40. J. Mayhew, D. Johnston, J. Berwick, M. Jones, P. Coffey, and Y. Zheng, "Spectroscopic Analysis of Neural Activity in Brain: Increased Oxygen Consumption Following Activation of Barrel Cortex," Neuroimage **12**(6), 664–675 (2000).
41. M. Jones, J. Berwick, D. Johnston, and J. Mayhew, "Concurrent optical imaging spectroscopy and laser-Doppler flowmetry: the relationship between blood flow, oxygenation, and volume in rodent barrel cortex," Neuroimage **13**(6), 1002–1015 (2001).

#191636 - $15.00 USD Received 3 Jun 2013; revised 4 Sep 2013; accepted 5 Sep 2013; published 4 Oct 2013

42. A. W. Bero, A. Q. Bauer, F. R. Stewart, B. R. White, J. R. Cirrito, M. E. Raichle, J. P. Culver, and D. M. Holtzman, "Bidirectional Relationship between Functional Connectivity and Amyloid-β Deposition in Mouse Brain," J. Neurosci. **32**(13), 4334–4340 (2012).
43. B. R. White, A. Q. Bauer, A. Z. Snyder, B. L. Schlaggar, J.-M. Lee, and J. P. Culver, "Imaging of functional connectivity in the mouse brain," PLoS ONE **6**(1), e16322 (2011).
44. K. J. Friston, J. T. Ashburner, S. J. Kiebel, T. E. Nichols, and W. D. Penny, *Statistical Parametric Mapping: The Analysis of Functional Brain Images*, 1st ed. (Academic Press, 2006).
45. V. Latora and M. Marchiori, "Efficient Behavior of Small-World Networks," Phys. Rev. Lett. **87**(19), 198701 (2001).
46. S. Achard and E. Bullmore, "Efficiency and Cost of Economical Brain Functional Networks," PLOS Comput. Biol. **3**(2), e17 (2007).
47. D. S. Bassett and E. Bullmore, "Small-world brain networks," Neuroscientist **12**(6), 512–523 (2006).
48. S. Whitfield-Gabrieli and A. Nieto-Castanon, "Conn: a functional connectivity toolbox for correlated and anticorrelated brain networks," Brain Connect **2**(3), 125–141 (2012).
49. F. Pukelsheim, "The Three Sigma Rule," Am. Stat. **48**, 88 (1994).
50. J. Saramäki, M. Kivelä, J.-P. Onnela, K. Kaski, and J. Kertész, "Generalizations of the clustering coefficient to weighted complex networks," Phys. Rev. E Stat. Nonlin. Soft Matter Phys. **75**(2), 027105 (2007).
51. P. Thevenaz, U. E. Ruttimann, and M. Unser, "A pyramid approach to subpixel registration based on intensity," IEEE Trans. Image Process. **7**(1), 27–41 (1998).

## 1. Introduction

Arterial hypertension is a non-communicable disease with prevalence between 25% and 30% of the world adult population [1] and is a risk factor in early brain aging, the development of cognitive dysfunctions and dementias. Cognitive deficits, including non-amnesic mild cognitive impairment [2], have also been associated with coronary heart diseases (CHD) [3–5]. Hardening of the arteries has been identified as a risk factor in the development of cardiovascular disease (CVD) and may play a role in the development of such deficits. Arterial stiffness has been shown to be a predictor of cognitive decline and dementia [6]. Basic cognitive functions such as attention and memory are also adversely affected by aging [7], a process accelerated by risk factors for CVD.

Anatomic and functional brain imaging are actively used to investigate such changes to brain function. Imaging correlates of aging and age-induced cognitive deficits include a decrease in connectivity and efficiency of functional brain networks [8], smaller brain volume and weight [9,10] and a reduction in cerebral blood flow (CBF) [11,12] related to endothelial dysfunction [13,14]. While the above investigations suggest a potential for functional brain imaging techniques in the clinical setting, they remain hampered by interpretation difficulties. A key step forward is to understand the impact of systemic physiology and vascular hardening and/or stenosis on functional imaging brain signals derived from hemodynamics.

While functional MRI (fMRI) studies used in basic research to explore brain organization have focused on the brain's response to a task; the complexities of task design, the duration of multiple trials, interpretation and statistical analysis have limited their use in extensive clinical studies. Resting-state networks (RSN) with fMRI eases the participation of the subject, and reduce the number of behavioral variables implicit in task-based paradigms, yielding a set of basic networks that can be reliably imaged in human subjects [15–18]. The application of RSN mapping with fMRI to diverse neuroscience research areas has revealed new insights in the organization of both healthy [19,20] and diseased brain, such as Alzheimer's [18,21–23]. RSNs have unraveled potential mechanisms of the brain in several areas, but the concrete meaning of the underlying processes and their interpretation remain to be resolved. Characterizing RSNs in the presence of vascular disease is a first step to establish RSN techniques in this context and may explain the scarcity of RSN studies in vascular pathology. Both increases and decreases in functional connectivity in vascular cognitive impairment were found by Sun et al. [24]. Resting-state connectivity has been included in the RUN DMC study of cerebral small vessel disease [25], a project recently begun. Recently, distinct patterns of RSN disruptions correlated with diminished cognitive performance in patients with carotid stenosis [26].

#191636 - $15.00 USD Received 3 Jun 2013; revised 4 Sep 2013; accepted 5 Sep 2013; published 4 Oct 2013

The current work exploits the recent development of a controlled murine arterial stiffness model induced unilaterally by the application of calcium chloride ($CaCl_2$). In previous work [27], this model was shown to induce neuronal degeneration in the hippocampus. To further reveal the impact of carotid artery calcification and increased stiffness on the brain, blood flow pulsatility in small arteries was quantified in both hemispheres. Statistically significant changes in pulsatility were observed on the $CaCl_2$ group, suggesting that carotid stiffness had an impact on the pulsatile component of blood delivery but none were observed on baseline flow. This model, whereby one can study the isolated effect of unilateral carotid calcification on the brain, provides a unique opportunity to investigate the specific impact arterial hardening on resting state networks.

The current study aims to assess resting-state connectivity in this unilateral carotid stiffness murine model using multi-spectral intrinsic optical imaging. Using multiple illumination wavelengths, relative changes in $HbO_2$ and HbR can be estimated, while speckle imaging provides access to relative CBF. This then enables estimations of $CMRO_2$. Hence, due to access to distinct hemodynamic components, functional connectivity based on optical imaging of intrinsic signals (fcOIS) may provide additional information that complements resting-state studies with fMRI in the context of vascular disease.

## 2. Materials and methods

### *2.1 Animal model*

A total of N = 23 Male C57BL/6 mice (8 ± 0.2 weeks old, 23.6 ± 1.4 g weight, Charles River, Wilmington, MA), divided in two groups were used in this study. Animal carotids were exposed and submitted to a sham procedure (Group 1, N = 11), where a sterile NaCl 0.9% solution was applied to the carotid or the calcification procedure (Group 2, N = 12) with a 0.3M $CaCl_2$ solution applied. The Animal Research Ethics Committee of the Montreal Heart Institute approved all surgical procedures, which were performed according to the recommendations of the Canadian Council on Animal Care.

#### 2.1.1 Application of calcium chloride

Applying calcium chloride periarterially developed carotid stiffness *in vivo*. Male C57BL/6 mice (8 ± 0.2 weeks old, 23.7 ± 1.6 g weight) were anaesthetized with isoflurane (5% for induction, 2% for maintenance) in oxygen (2 L/min for induction, 1.5 L/min for maintenance). The procedure required 45 minutes of anesthesia per animal and body temperature was controlled between 36 and 37 °C using a heating blanket (MouseSTAT, Kent Scientific, Torrington, CT). A midline incision was performed in the neck and the right common carotid artery (RCCA) was isolated, then a sterile cotton gaze soaked in either sterile NaCl 0.9% solution for the control group (N = 11) or with a 0.3M $CaCl_2$ solution for the treated group (N = 12) was applied to the carotid artery for twenty minutes. Afterwards the skin incision was closed with sutures and sealed with tissue adhesive (Vetbond, 3M, St. Paul, MN). Bupivacaine (Marcaine) (4mg/kg) and Carprofen (5 mg/kg) were administered subcutaneously (SC) to provide post-surgical local anesthesia. Furthermore, Carprofen (5 mg/kg SC) was injected every 24 hours for 48 hours and on the third day if deemed necessary. Infections were effectively prevented with the administration of trimethoprim-sulfamethoxazole (Tribrissen, 30 mg/kg SC) post-operatory and every 24 hours for 3 to 5 days. Animals were monitored twice a day during the first postoperative week and assessed for body weight, symptoms of local infection, discomfort or pain, behavior, and water and food consumption. Following this recovery period, mice were monitored daily. Optical imaging of intrinsic signals (OIS) was performed two weeks after the surgical procedure.

#191636 - $15.00 USD Received 3 Jun 2013; revised 4 Sep 2013; accepted 5 Sep 2013; published 4 Oct 2013

### *2.2 OIS Imaging*

#### 2.2.1 Animal preparation

Mice were anesthetized via intraperitoneal injections of urethane (2mg/g body weight) in a 10% (wt/vol) saline solution. Body temperature was maintained at 36.6 ± 1.2°C with a feedback controlled heating blanket. A tracheotomy was done in order to avoid respiratory distress [28]. Scalp was carefully removed prior to imaging.

Mice were placed on a stereotaxic apparatus and a subcutaneous electrocardiogram was recorded with a single lead ECG amplifier (amp-b01, emka TECHNOLOGIES, Paris). The amplified (1000 × gain) and filtered signal (0.2-500 Hz) was sampled at 1 kHz. All vital signals were digitized by a data acquisition card (NI-USB 6353, National Instruments, Austin, TX) controlled by a custom made graphical user interface developed in LabView (National Instruments), which also controlled the image acquisition. To prevent drying of the exposed skull a custom chamber made of bone wax was adhered to the skull with ultrasound gel and filled with mineral oil.

#### 2.2.2 Optical recording setup

OIS images were acquired with a 12-bit CCD camera (Pantera 1M60, DS-21-01M60-12E, Teledyne Dalsa, Waterloo, ON) with a pixel size on chip of 12μm and full resolution of 1024 × 1024 pixels. The setup used in this work is depicted in Fig. 1(a).

A custom-made interface controls the camera, records images and vital signs, while synchronizing acquisition and illumination. A Macro Lens (105mm f/2.8max, Sigma Corp., Ronkonkoma, NY) with small focal depth (350 μm) was used. Reflectance images of the brain were recorded with time-multiplexed illumination (525, 590, 625 nm) produced by 10W LEDs (LZ4-00MA00, Led Engin, San Diego, CA). Illumination for speckle imaging was provided by a 90 mW, 785 nm laser diode (L785P090, Thorlabs, Newton, NJ) and the camera aperture was adjusted to f/8, so that the pixel size and speckle size were matched. The four temporally multiplexed wavelengths led to a full-frame rate of 5 Hz. A 2 × 2 binning on camera was performed to allow continuous data streaming to the hard drive. The camera field of view (FOV) was set to ~10.1 × 10.7 mm in order to cover most of the convexity of the cortex; the image pixel size for the chosen FOV was approximately 33μm. Illumination was further adjusted so that no part of the brain was under- or over-saturated by any of the wavelengths. The exposure time of the camera was set to 10 msec. The setup was mounted on an optic table with tuned damping (RS 2000, Newport, Irvine, CA) to avoid spurious signals from vibrations.

#191636 - $15.00 USD Received 3 Jun 2013; revised 4 Sep 2013; accepted 5 Sep 2013; published 4 Oct 2013

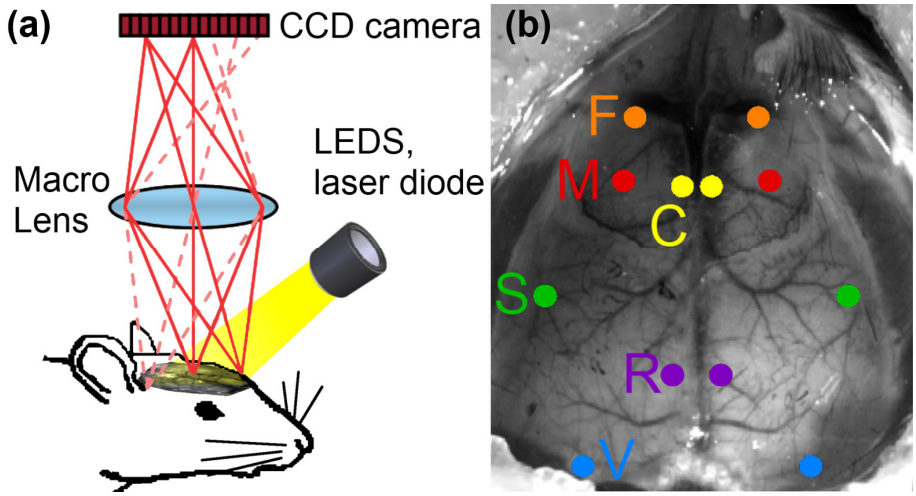


Fig. 1. (a) Overview of the intrinsic signal optical imaging system. LEDs and laser diode are time-multiplexed and synchronized to the acquisition system so that each recorded image corresponds to either a single LED wavelength (525, 590, 625 nm) or to the laser illumination (785 nm). (b) Functional regions on the mouse cortex and seed placement and size, manually constructed from the work of Bero et al. [42]. Abbreviations: F, frontal; M, motor; C, cingulate; S, somatosensory; R, retrosplenial; V, visual.

2.2.3 OIS processing

The analysis of spectroscopic images was based on previously published work [29,30]. In short reflectance images from each LED wavelength were recorded with the CCD camera and interpreted as changes in attenuation (optical density) $\Delta OD = \log(I_0/I)$, where $I$ is the reflected light intensity and $I_0$ the incident light intensity. Relative changes in oxy- and deoxyhemoglobin were found using the modified Beer-Lambert law [31] and a Moore-Penrose pseudoinverse:

$$\Delta OD(\lambda,t) = \sum_i \varepsilon_i(\lambda) C_i(t) D(\lambda). \quad (1)$$

The differential path length factor, $D(\lambda)$, was taken from [32] and values out of the 560-610 nm range were extrapolated from [33]. Total hemoglobin baseline concentration of 100 μM with 60% oxygen saturation was assumed [32] for the spectroscopic analysis. The hemoglobin extinction coefficients were obtained from [34] and the reflectance values were corrected for the spectral response of the CCD camera and convolved with the LEDs spectral power distribution [35].

Images of each chromophore ($HbO_2$, HbR) were spatially smoothed with a Gaussian kernel of 11 × 11 pixels (~0.3 × 0.3mm) with a 5 pixel standard deviation (~0.15mm). An anatomical image was recorded with illumination at 525 nm to emphasize vasculature, and then the region corresponding to the brain was manually selected using a closed spline curve to create a brain mask. All further processing was performed only on those pixels belonging to the brain mask.

2.2.4 Speckle contrast imaging

In addition to imaging changes in hemoglobin concentrations, changes in cerebral blood flow (CBF) were also computed by laser speckle contrast imaging [32,36,37]. Images of blood flow were obtained by measuring the spatial contrast of the speckle $C$, defined as the ratio of the standard deviation to the average intensity $\sigma/\langle I \rangle$ [38]. A window of 5 × 5 pixels (0.15 ×

#191636 - $15.00 USD Received 3 Jun 2013; revised 4 Sep 2013; accepted 5 Sep 2013; published 4 Oct 2013

0.15mm) was used to compute the speckle contrast images and the relative changes in blood flow were obtained with the following formula:

$$C = \frac{\sigma}{\langle I \rangle}, \frac{2\Delta C}{C_0} \approx \frac{\Delta v}{v_0} \approx \frac{\Delta CBF}{CBF_0}, \quad (2)$$

The quantity $\Delta v / v_0$ is not directly related to CBF, however laser speckle imaging underestimates CBF by less than 5% [39], so both quantities were assumed to be equal in this work. Flow images then underwent the same spatial filtering as the hemoglobin images, and images from all three different contrasts were further resized to ½ of the original size due to memory constraints.

2.2.5 Cerebral metabolic rate of oxygen

Changes in the cerebral metabolic rate of oxygen consumption ($CMRO_2$) were calculated from the images of changes in CBF, total hemoglobin (HbT) and HbR using the steady state relationship [40,41]:

$$\frac{\Delta CMRO_2}{\Delta CMRO_{2,0}} = \frac{\left(1+\frac{\Delta CBF}{CBF_0}\right)\left(1+\gamma_R \frac{\Delta HbR}{HbR_0}\right)}{\left(1+\gamma_T \frac{\Delta HbT}{HbT_0}\right)} - 1, \quad (3)$$

A central hypothesis of this relation is the absence of transients with decoupled hemodynamic components. Here, since resting state networks were identified from data filtered between 0.009 and 0.08 Hz, we hypothesized that for these networks, the relationship was maintained. The constants $\gamma_R$ and $\gamma_T$ where both assumed to be 1, which is within a physiologically plausible range (0.75–1.25) [41].

*2.3 Resting state network analysis*

2.3.1 Seed based functional connectivity

Optical recording sessions of 15 minutes were carried out in resting-state conditions for the fcOIS analysis. Time courses of every pixel were temporally band-pass filtered (zero phase-shift fourth-order Butterworth IIR filter) at 0.009-0.08 Hz, according to previous functional connectivity studies in mice [42,43]. After temporal filtering, each pixel time trace was downsampled from 5 Hz to 1 Hz.

A global brain signal was created from the average of all the pixels time traces. In order to account for coherent variability common to all pixels, this global brain signal was regressed from every pixel's time course, using a General Linear Model (GLM) from the package Statistical Parametrical Mapping [44] (SPM8, www.fil.ion.ucl.ac.uk/spm) running on MATLAB (The MathWorks, Natick, MA).

All seeds were manually placed a priori using the coordinates corresponding to left and right frontal, cingulate, motor, somatosensory, cingulate and visual cortices, as shown on Fig. 1(b). Manual positioning of the seeds was done in order to avoid contributions from large vessels. Seed time-courses were computed as the mean time course of the pixels within a 7 pixel (~0.23mm) radius from the seed locus.

With the unilateral application of $CaCl_2$ we expect differences between bilateral brain regions so the metric used to evaluate functional connectivity was a regional bilateral functional correlation, defined as the correlation between each seed time course and its contralateral homologue, yielding six values for each mouse. The Pearson's coefficient r-values were converted to Fisher Z measures using $z(r) = \frac{1}{2}\ln\left[(1+r)/(1-r)\right]$ before performing the random effect t-tests. Statistical significance was evaluated using the

#191636 - $15.00 USD Received 3 Jun 2013; revised 4 Sep 2013; accepted 5 Sep 2013; published 4 Oct 2013

Student's unpaired t-test. Values were considered significant at $p<0.05$, adjusted for false discovery rate (FDR).

2.3.2 Graph theoretical measures

Several graph theoretical measures were computed in addition to assess the potential impact of the carotid calcification on the topological properties of the brain networks. While these measures do not provide clear informative information about function, they yield indicators of network changes that may occur with arterial stiffness. The brain was modeled as a graph where the nodes (*N*) were associated with seeds and edges (*K*) were associated with the amplitude of functional connectivity *z(r)* among these seeds [45]. Following the computation of seed-to-seed connectivity matrix, a threshold was applied to define the adjacency matrix characterizing the graph *G*. A cost threshold level of 0.3 was chosen at which the network exhibited small-world properties, characteristic of brain functional networks [46,47].

Several properties of brain organization were investigated through the proxy of graph measures at seed level [47,48]: 1) the degree $k_n(G)$, defined as the number of edges that connect to a certain node *n*. 2) the cost $C_n(G)$, defined as the proportion of connected neighbors to a given seed. 3) The average path length $L_n(G)$ is defined as the average shortest-path distance from a node *n* to all other nodes in the graph, 4) the global efficiency $E_n^{global}(G)$, which is the average inverse shortest-path distance from node *n* to all other vertices in the graph. 5) The clustering coefficient $CC_n(G)$, defined as the probability that the neighbors of this node are also connected to each other; 6) the local efficiency $E_n^{local}(G)$, defined as the average global efficiency across all neighbors of node *n*. Finally, 7) the betweenness centrality $CB_n(G)$ of a particular node *n* is the proportion of all shortest-paths in a network that pass through this node.

Averaging seed-level measures across all nodes within the network generated measures reflecting the global integration in the network. These summary network-level measures were entered in a second-level general linear model to compare functional connectivity patterns between the control (NaCl) and the $CaCl_2$ groups. Statistical significance was determined by a Student's unpaired t-test ($p<0.05$) with false discovery rate (FDR) correction. All the graph theoretical measures were performed with the CONN functional connectivity toolbox [48].

## 3. Results

No signs of infection at the incision site, weight loss, or discomfort were observed during daily inspections throughout the post-operatory period. Two animals of the $CaCl_2$ group deceased prior to the imaging session, possibly due to incorrect positioning of the tracheotomy tube, which hampered normal breathing. One more animal of the same group was not included in the analysis due to poor quality data caused by unwanted saturation outside the region of interest, which in turn saturated a whole line of the CCD camera. The final sample size used for all analyses was N = 9 for $CaCl_2$ group and N = 11 for NaCl (control) group.

### *3.1 Seed-based functional connectivity*

Average seed-based correlation maps across animals for $HbO_2$ are depicted in Fig. 2. The first two columns belong to the control (NaCl) group, while the last two columns are from the $CaCl_2$ group. Every row contains maps generated from a seed located in a different cortical region, first using the seed located in the left hemisphere and then its contralateral homologue. The $CaCl_2$ group showed a greater spatial extent of high positively correlated pixels, when compared to the NaCl group ($CaCl_2$ = 7.6% ± 3.6% vs. NaCl = 5.14% ± 1.63%,

#191636 - $15.00 USD Received 3 Jun 2013; revised 4 Sep 2013; accepted 5 Sep 2013; published 4 Oct 2013

p = 0.0278) with the spatial extent defined as the percentage of pixels showing a correlation coefficient greater than 0.5. Representative fc maps of other contrasts are shown in Fig. 5.

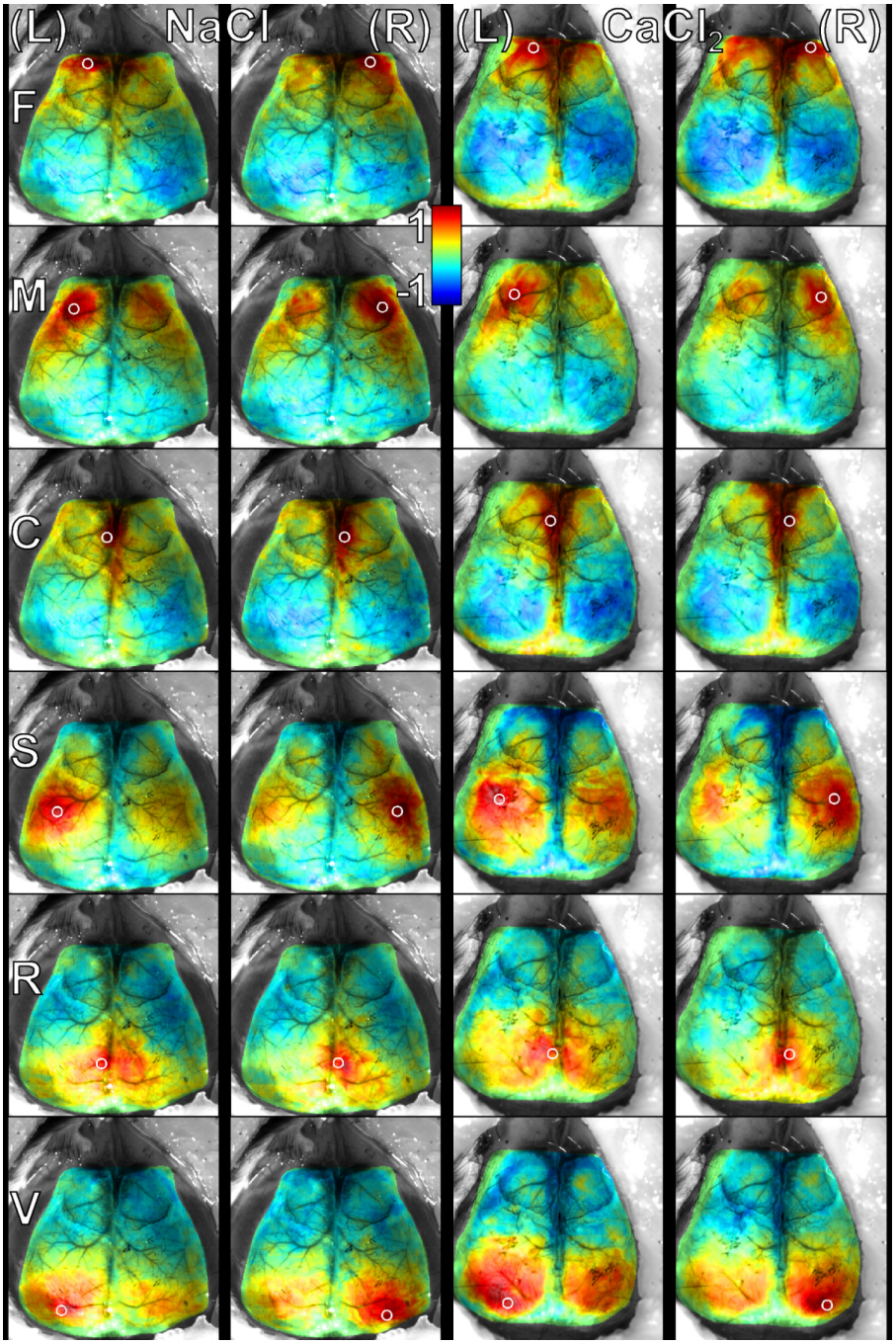


Fig. 2. Average seed-based correlation maps. Images were manually aligned through an affine registration using ImageJ's plugin TurboReg [51]. $HbO_2$ contrast is shown. The scale for all correlation maps is $-1 \leq r \leq 1$. Maps are shown overlaid on the anatomical image of one of the mice for reference ($\lambda = 525$ nm). White circles denote seed position and size. Abbreviations: F: frontal cortex, M: motor cortex, C: cingulate cortex, S: somatosensory cortex R: retrosplenial cortex, V: visual cortex, (L) left seed, (R) right seed.

#191636 - $15.00 USD Received 3 Jun 2013; revised 4 Sep 2013; accepted 5 Sep 2013; published 4 Oct 2013

$HbO_2$ contrast Fig. 3(a) data displayed mostly non-significant changes of bilateral functional correlation *z(r)* in $CaCl_2$ mice when compared to controls. A decrease was seen in the seeds of the frontal, motor and retrosplenial cortex, while an increase was noted in the cingulate, somatosensory and visual regions. HbR (Fig. 3(b)) data showed diminished *z(r)* in all regions except in the visual cortex where it increased, albeit not significantly. CBF (Fig. 3(c)) data showed overall a smaller *z(r)* values in all cortical regions. This might be explained by a greater variance in CBF seeds time traces associated with a noisier recording of the speckle signal. With this contrast the seeds that showed a smaller *z(r)* in the $CaCl_2$ mice were located in the motor, cingulate and somatosensory regions of the cortex. Frontal, retrosplenial and visual cortex seeds showed a slightly larger *z(r)* in the $CaCl_2$ group, when compared to NaCl mice. $CMRO_2$ (Fig. 3(d)) data showed a general trend of decreased functional connectivity *z(r)* in the mice that underwent $CaCl_2$ procedure, except in frontal cortex seeds. Decreased connectivity showed a trend in the motor ($p = 0.1241$) and cingulate ($p = 0.1241$) regions..

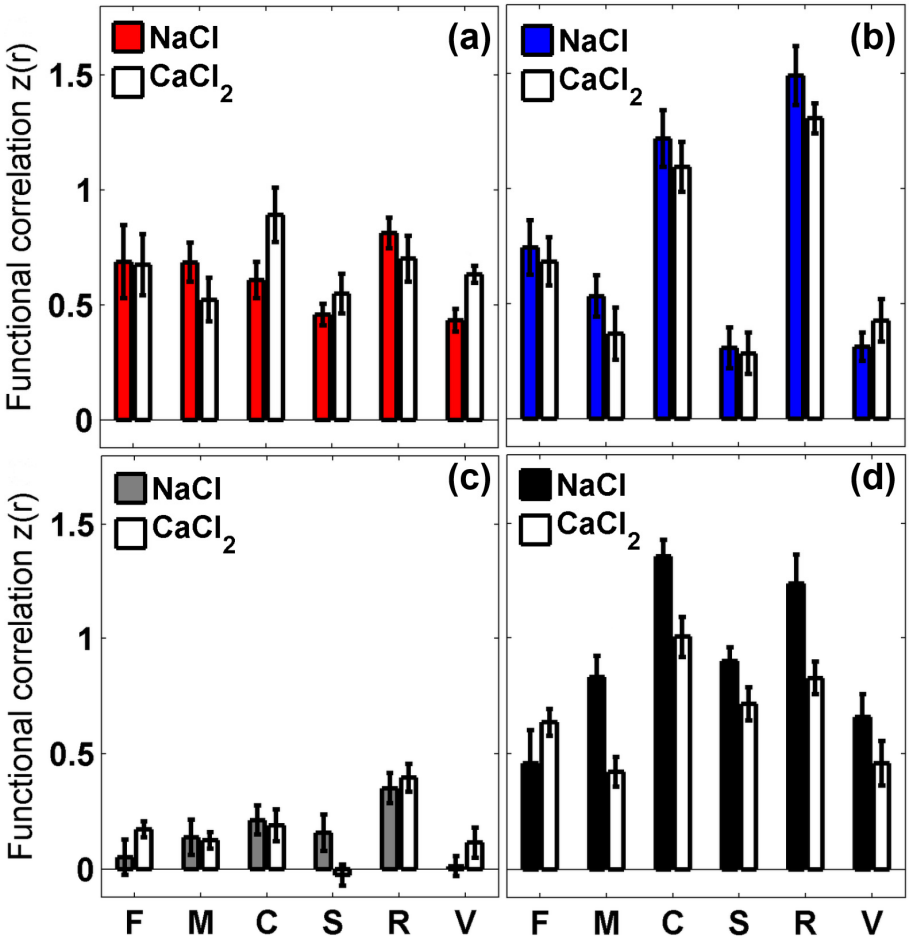


Fig. 3. Regional bilateral functional correlation, comparison performed between control NaCl and treatment group $CaCl_2$; analysis done for every seed time-trace and its contralateral part. Contrasts shown: (a) $HbO_2$, (b) HbR (c) CBF and (d) $CMRO_2$. Standard error bars shown (F: frontal cortex, M: motor cortex, C: cingulate cortex, S: somatosensory cortex R: retrosplenial cortex, V: visual cortex).

#191636 - $15.00 USD Received 3 Jun 2013; revised 4 Sep 2013; accepted 5 Sep 2013; published 4 Oct 2013

To further explore the robustness of observed bilateral functional connectivity, a second analysis was performed, where data points that were more than 3 standard deviations away from the mean were considered outliers and excluded [49]. Results obtained after outlier removal are shown in Fig. 6, results remain very similar to the full data set, with $HbO_2$ data for visual cortex and $CMRO_2$ data in motor and cingulate regions showing the same trends.

*3.2 Graph theoretical measures*

In $HbO_2$ measures, we found significant differences in the global network measures in the betweenness centrality and average path length, which were both higher for the NaCl group. When looking at the topological properties of each seed we found differences (although not significant when FDR corrected) in global, local efficiency, betweenness centrality, average path length and clustering coefficient.

**Table 1. Summary of significant results from second-level analysis using graph theoretical measures [a]**

| | ROI level | | | | | Network level | | | |
|---|---|---|---|---|---|---|---|---|---|
| | **$HbO_2$** | **HbR** | **CBF** | **$CMRO_2$** | | **$HbO_2$** | **HbR** | **CBF** | **$CMRO_2$** |
| $E_n^{global}(G)$ | $M_R$ | | $M_L$,$F_L$ $M_R$ | | $E^{global}(G)$ | | | * | |
| $E_n^{local}(G)$ | $F_R$ | | $M_R$, $R_L$, $V_R$ | | $E^{local}(G)$ | | | * | |
| $CB_n(G)$ | $M_L$ | | **$M_R$*** | | $CB(G)$ | * | | * | |
| $C_n(G)$ | | $M_L$ | | $C_L$ | $C(G)$ | | | | |
| $L_n(G)$ | $S_R$,$S_L$,, $F_R$,,$F_L$, $C_L$ | $S_L$ | $F_R$,$V_R$ | | $L(G)$ | * | | * | |
| $CC_n(G)$ | $F_R$ | | ***$M_R$*,** $R_L$, $V_R$ | | $CC(G)$ | | | * | |
| $k_n(G)$ | | $M_L$ | | $C_L$ | $k(G)$ | | | | |

[a]Subscripts indicate hemisphere (Left/Right). Increase in the $CaCl_2$ group with respect to NaCl group is shown in red font, while decrease is shown in cursive blue font. Bold font and * indicate FDR-corrected p values at a 0.05 significance level. Measurements abbreviations: global efficiency $E_n^{global}(G)$, local efficiency $E_n^{local}(G)$, betweenness centrality $CB_n(G)$, cost $C_n(G)$, average path length $L_n(G)$, clustering coefficient $CC_n(G)$ and degree $k_n(G)$. Regions abbreviations: F: frontal cortex, M: motor cortex, C: cingulate cortex, S: somatosensory cortex R: retrosplenial cortex, V: visual cortex

At the network-level there were no significant differences in HbR measures, but at ROI level the left motor seed showed significant (not FDR-corrected) differences in cost and degree. Also the left somatosensory seed showed increased average pathlength.

Graph analysis based on CBF data showed significant increase in the global efficiency, betweenness centrality and average pathlength; significant decreases were found in local efficiency and clustering coefficients. At seed level there was a significant increased betweenness centrality and clustering coefficient for the right motor seed. Some differences were also found at seed level, although not significant when FDR corrected in global and local efficiency, average path length and clustering coefficient.

Using $CMRO_2$ estimates increased clustering and degree were found to be significant (not FDR-corrected) in the left cingulate seed; although no significant differences were found with $CMRO_2$ measures at network level.

The results above were based on binarized networks. Extending these results, Fig. 4 reports results for weighted networks, displaying the average strength of connections for both

#191636 - $15.00 USD Received 3 Jun 2013; revised 4 Sep 2013; accepted 5 Sep 2013; published 4 Oct 2013

groups; with node sizes proportional to their betweenness centrality $CB_n(G)$, a measure of the relative importance of a seed in the network. Few evident changes in the overall connectivity can be inferred from visual inspection of hemoglobin and CBF networks alone. However, the connectivity changes in $CMRO_2$ are more evident: a large number of nodes are anticorrelated and most of the positive edges did not survive the threshold in the $CaCl_2$ group, when compared to the control group.

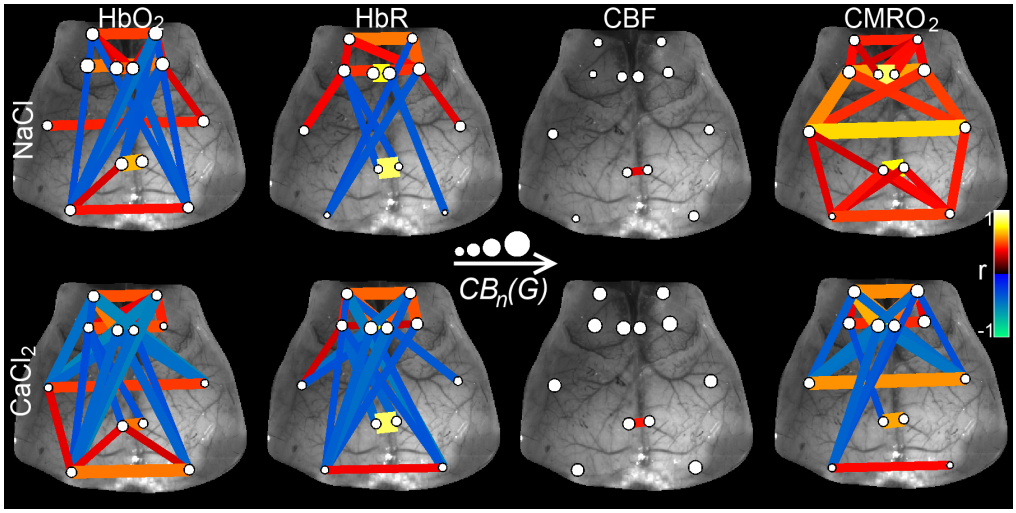


Fig. 4. Functional connectivity diagrams for NaCl (top row) and $CaCl_2$ (bottom row) subjects. Edge thicknesses depend on the seed-to-seed average correlation coefficients, only edges with |r|>0.3 are shown. Node sizes are proportional to betweenness centrality $CB_n(G)$ of each seed. Positive correlations are depicted in warm colors. Negative correlations are depicted in cool colors.

## 4. Discussion

The goal of this work was to investigate the impact of controlled unilateral carotid stiffness on resting state networks in anesthetized mice. While an increasing number of studies suggest that arterial stiffness is a risk factor predictive of ensuing cognitive dysfunction with age, its role in modulating functional hemodynamic imaging remain difficult to assess, mainly due to a lack of animal model in the past to isolate its effect. Blood flow coming from the carotids feeds the circle of Willis and typically represents 70% of the total cerebral perfusion. Amongst regions selected for our analysis, we expect that the occipital cortex (visual) as well as part of the temporal and parietal cortices to receive diminished output from the affected carotid when compared to others.

### *4.1 Hemodynamic changes*

The observed changes of correlation maps spatial extent reflect a spatial reorganization of the hemodynamic-derived functional connectivity within the cortex. For individual seeds, significant larger spatial areas of contra-lateral coherent hemodynamic fluctuations were observed in the $CaCl_2$ group. We can speculate that this mechanism originates in the physiological response to the modified pulse wave from the rigidified carotid to the circle of Willis, potentially inducing a global response from resistance arteries. In a separate study (in-progress) we observed changes in flow mediated dilation and myogenic tone in pressurized isolated arteries subject to different levels of pulsatility, supporting this mechanism as a vascular modulator of connectivity changes independent of metabolism

Focusing on the seed location and correlation amplitude rather than the correlation extent, results from $HbO_2$, HbR and CBF measures show that compared to the NaCl group, the $CaCl_2$

#191636 - $15.00 USD Received 3 Jun 2013; revised 4 Sep 2013; accepted 5 Sep 2013; published 4 Oct 2013

group had decreased bilateral correlation values within the motor cortex but increased bilateral correlations within the visual cortex. In other seeds, depending on the hemodynamic component and spatial location, changes in bilateral correlations going in both directions (increase and decrease) suggest interplay between systemic hemodynamic changes when blood supply is unilaterally manipulated and loss of neuronal synchrony from neural degeneration in the hippocampus previously observed in this model. Overall results from evaluations of the bilateral synchrony underline the importance of careful interpretation when using a single hemodynamic signal as a proxy for neural changes is situations where blood supply is compromised.

### *4.2 $CMRO_2$*

Amongst important findings, $CMRO_2$ functional connectivity changes did not always correspond to changes observed in the other contrasts. In fact, when looking at homologous correlations, $CMRO_2$ results were different in 50% of the analyzed seeds, with respect to CBF, $HbO_2$ and HbR changes. $CMRO_2$ indicated a decreasing trend of functional connectivity in the $CaCl_2$ group that was more evident in the motor and cingulate regions. Since $CMRO_2$ potentially displays increased independence to vascular changes and provides a metabolic measure expected to closely match neural activity, observed changes may better reflect hippocampal neurodegeneration observed previously in this model. Using fcOIS based on hemoglobin absorption only we would not be able to discern the vascular response from the underlying metabolic activity, hence the need for a more complete set of hemodynamic parameters. These results further support that care must be taken when interpreting functional connectivity studies with techniques that solely rely on hemodynamics.

### *4.3 Graph theoretical measures*

When looking at seed level, RCCA stiffness proved to have the most impact on network measures in the right frontal cortex, in both $HbO_2$ and CBF measures. Local efficiency and clustering coefficient, both measures of network robustness were significantly higher in the NaCl group, potentially indicating loss of network efficiency due to the application of $CaCl_2$. The decrease in whole cortex average clustering coefficient can be interpreted as a reflection of the randomization of the functional networks with arterial stiffness; this randomization is particularly remarkable in the right motor cortex. Betweenness centrality was higher in the $CaCl_2$ group suggesting a more central hub role of the motor right regions in the general network structure. The non-significant differences in cost and degree in left motor seed (HbR) suggest that this node became more disconnected from the global network, with fewer neighbors in the $CaCl_2$ group. Cost and degree were also reduced in left cingulate seed in $CMRO_2$ measures, but these changes were not reflected at a global level.

Visual inspection of the weighted functional networks (Fig. 4) indicate a reorganization of the $CMRO_2$ networks, but due to the lack of a single formulation for weighted network measurements [50] their full characterization remains complex.

### *4.4 Impact for BOLD-fMRI*

Mapping resting-state networks provides an approach to assess brain function in populations where task-based fMRI scanning is challenging. The BOLD-fMRI signal arises from the magnetic properties of HbR, is dependent on local blood volume, flow and deoxygenation and is weighted towards venous vasculature. Our results show that investigating network connectivity solely based on HbR signals indeed showed decreased connectivity between homologous regions but these changes were not significant, weaker and only partially coherent with observations using $CMRO_2$. Globally, at the network level, HbR signals displayed small changes where compared to flow and $CMRO_2$. Overall, these results suggest that BOLD-fMRI signals may potentially be modulated by the rigidification of arterial

#191636 - $15.00 USD Received 3 Jun 2013; revised 4 Sep 2013; accepted 5 Sep 2013; published 4 Oct 2013

vasculature and benefit from combined flow and calibration measures in studies investigating resting state networks in populations affected by arterial stiffness.

## 5. Conclusion

Using a new carotid calcification murine model, we were able for the first time to investigate the isolated effect of unilateral carotid stiffness on resting state networks. It is difficult to make a direct comparison of our results to disease in humans and even other animal models, since our novel model is specific to study the role of carotid stiffness, independently of confounding variables, such as systemic changes in blood pressure, high levels of circulating lipids present in other models; or other factors leading to arterial stiffness in humans such as aging or atherosclerosis. Using multispectral fcOIS, our results show network modifications associated with the procedure and a potential uncoupling between hemodynamic measures (HbO, HbR and CBF) and metabolism ($CMRO_2$). While confounds remain due to the fact that the procedure leads to both neural degeneration in the hippocampus and lateral vascular alterations due to carotid rigidification, both of which will affect resting state networks, they underline the importance of calibration of brain images in the presence of arterial remodeling.

## Appendix

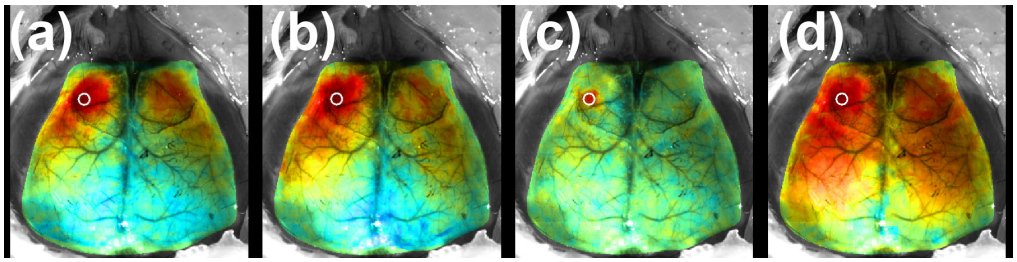


Fig. 5. Representative fc maps for all contrasts for a given seed ($M_L$) (a)$HbO_2$ (b)HbR (c) CBF (d) $CMRO_2$.

#191636 - $15.00 USD Received 3 Jun 2013; revised 4 Sep 2013; accepted 5 Sep 2013; published 4 Oct 2013

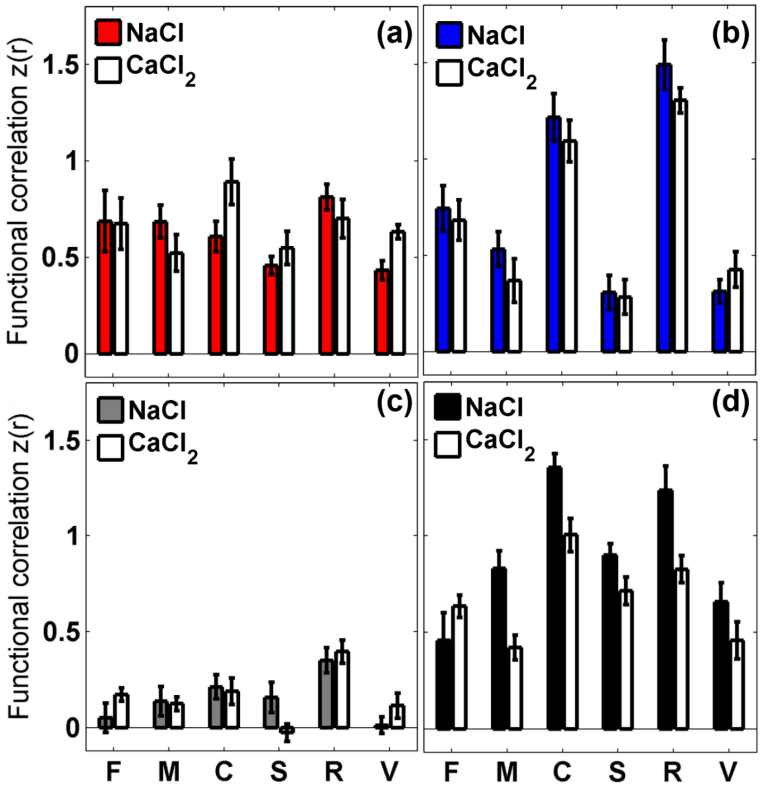


Fig. 6. Regional bilateral functional connectivity, comparison performed between control NaCl and treatment group $CaCl_2$; analysis done for every seed time-trace and its contralateral part. Data points that were more than 3 standard deviations away from the mean were considered outliers and consequently removed. Contrasts shown: (a) $HbO_2$, (b) HbR (c) CBF and (d) $CMRO_2$. Standard error bars shown ($\sigma/\sqrt{N}$), with N = 19. (F: frontal cortex, M: motor cortex, C: cingulate cortex, S: somatosensory cortex R: retrosplenial cortex, V: visual cortex).

**Acknowledgments**

The work described in this article was supported by NSERC Discovery Grant to F. Lesage and CONACYT scholarship No. 304501 to E. Guevara. The authors cordially thank Marc-Antoine Gillis for his assistance with animal preparation and Natacha Duquette for laboratory animal monitoring.